Supporting information for

Continuous Cavitation Designed for Enhancing Radiofrequency Ablation *via* a Special Radiofrequency Solidoid Vaporization Process

Kun Zhang,[†,¶] *Pei Li,*[†] *Hangrong Chen,*[‡] *Xiaowan Bo,*[†] *Xiaolong Li,*[†] *and Huixiong Xu**[†,‡,¶]

†Department of Medical Ultrasound, Shanghai Tenth people's Hospital, Tongji University School of Medicine, 301 Yan-chang-zhong Road, Shanghai, 200072, P. R. China; ‡ State Key Laboratory of High Performance Ceramic and Superfine Microstructures, Shanghai Institute of Ceramics, Chinese Academy of Science; 1295 Ding-Xi Road, Shanghai, 200050, P. R. China; ¶ Ultrasound Research and Education Institute, Tongji University School of Medicine, 301 Yan-chang-zhong Road, Shanghai, 200072, P. R. China.

* Address correspondence to xuhuixiong@126.com

Materials. Poly (lactic-co-glycolic acid) (50:50) with the molecular weight of 15,000 MW is purchased from Polyscience, USA. 1,1'-Dioctadecyl-3,3,3',3'-tetramethy-lindocarbocyanine perchlorate (Dil), DL-menthol (DLM) and Poly(vinyl alcohol) (PVA, MW=89,000-98,000) are purchased from Sigma-Adlrich. The chloroform and ethanol are purchased from Sinopharm Chemical Reagent Co., Ltd. Deionized water was used in all experiments.

Characterizations. TEM images were obtained by using JEM 2100 F electron microscope operating at 100 kV, and SEM images were obtained on a field-emission JEOL JSM-6700F microscope. The thermo-gravimetric (TG) and differential thermal analysis (DTA) are obtained by NETZSCH STA 449C. Hydrodynamic particle size is monitored by Zetasizer (Malvern, Nano-ZS90). Confocal images were obtained by using Olympus confocal microscopy. Raidofrequency ablation was conducted on a bipolar radiofrequency instrument, OLYMPUS Celon system (T20).Images and video of contrast-enhanced ultrasound imaging were obtained by using GE LogiQ E9 system with a 8 MHz transducer and Esaote MyLab™90 with a 10 MHz linear transducer, respectively. Thermal infrared images were obtained by using FLIR Sc300-Series. Confocal images were acquired on the OLYMPUS fluoview FV1000.

Supplementary Figures

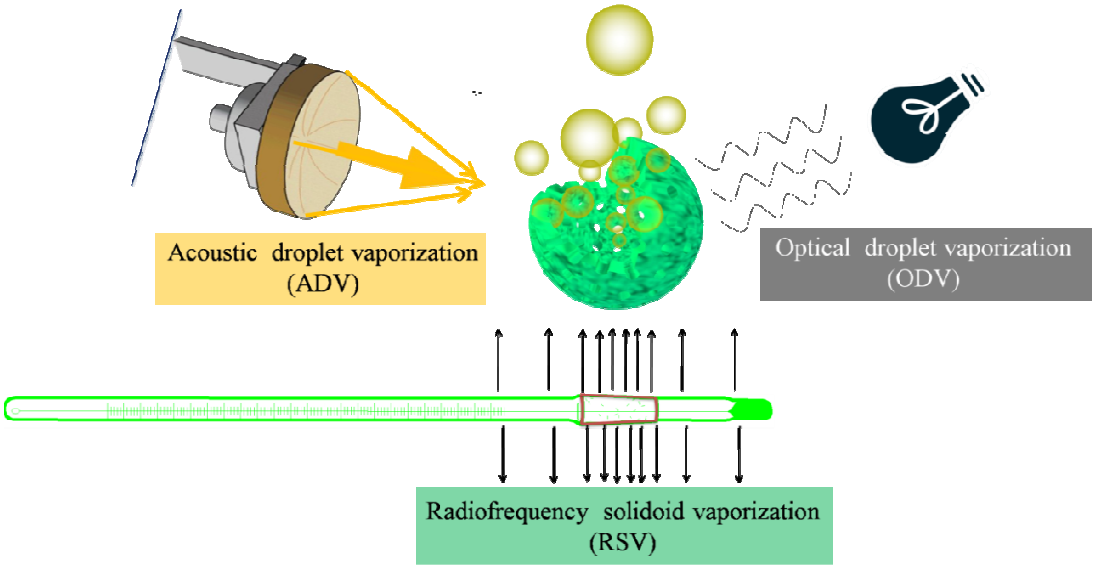

Figure S1. Schematic illustrations of ADV, ODV and RSV processes.

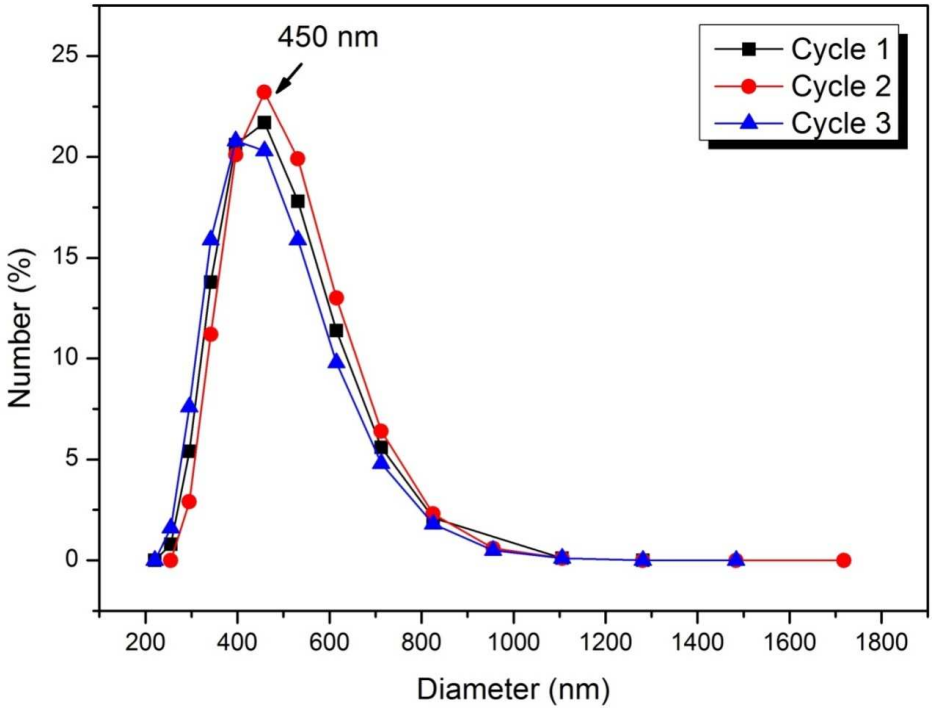

Figure S2. Particle size distribution of DLM@PLGA *via* the dynamic light scattering (DLS) method repeated for 3 times.

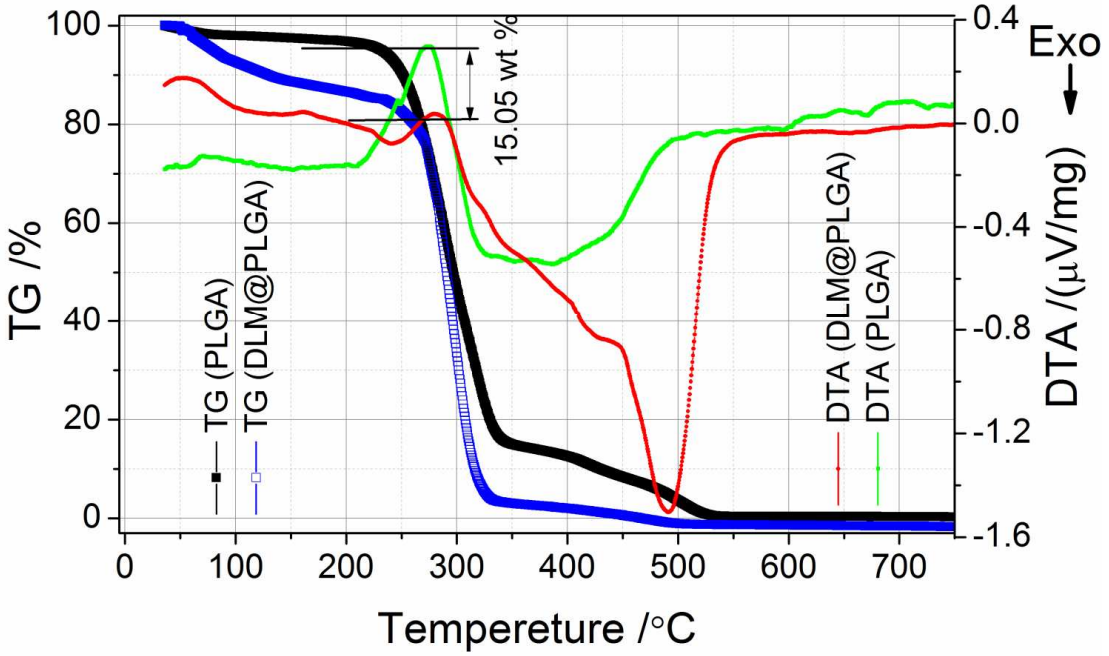

Figure S3. TG and DTA data of PLGA and DLM@PLGA with a heating rate of 10 ℃/min, wherein the evident differences in profiles of TG and DTA between PLGA and DLM@PLGA show the successful loafing of DLM in DLM@PLGA. Additionally, below 200 ℃, DLM@PLGA still exhibits a heat absorption process, while PLGA displays an exothermic process. This phenomenon shows the RSV process is always present below 200 ℃, which can promote continuous cavitation effect beneficial for the following contrast-enhanced ultrasound imaging and enhanced RF ablation.

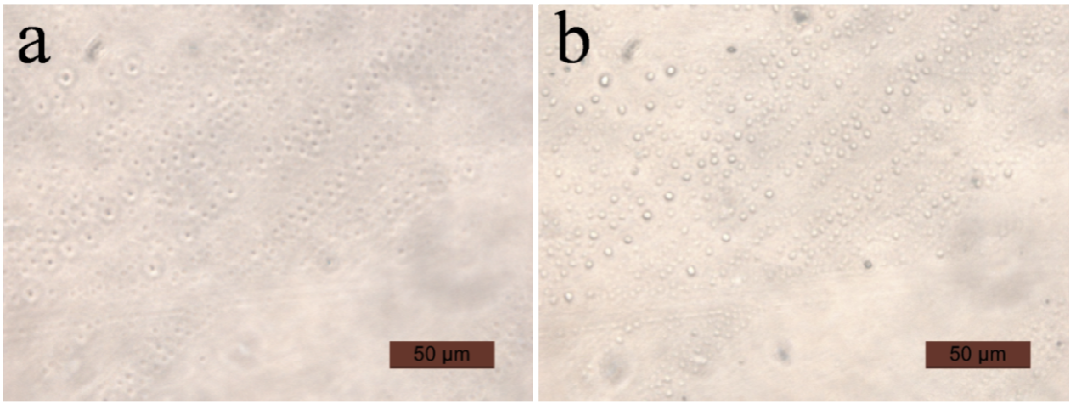

Figure S4.*In-situ* observation of RSV process. (a,b) Optical microscopic image of DLM@PLGA nanocapsules before (a) and after (b) RF heating.

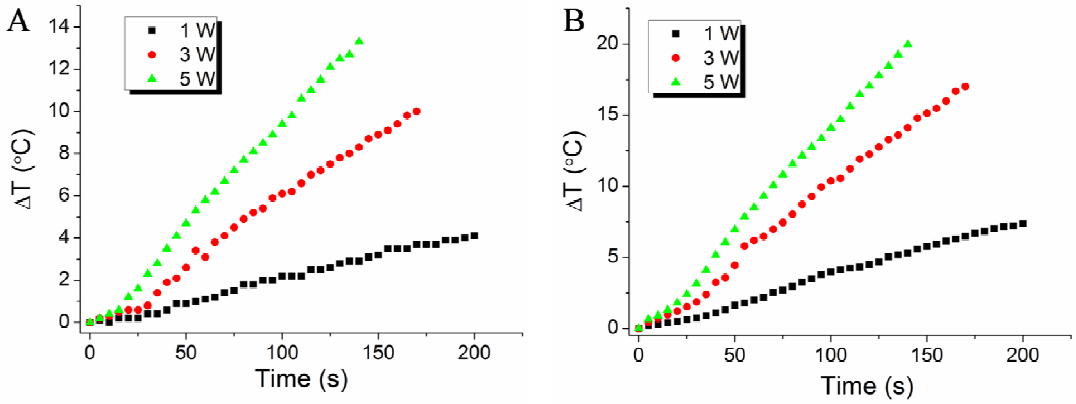

Figure S5. *In vitro* temperature variation profiles of egg albumen colloidal solution without (A) and with (B) adding DLM@PLGA (10 mg/mL) nanocapsules as a function of time exposure to RF irradiations.

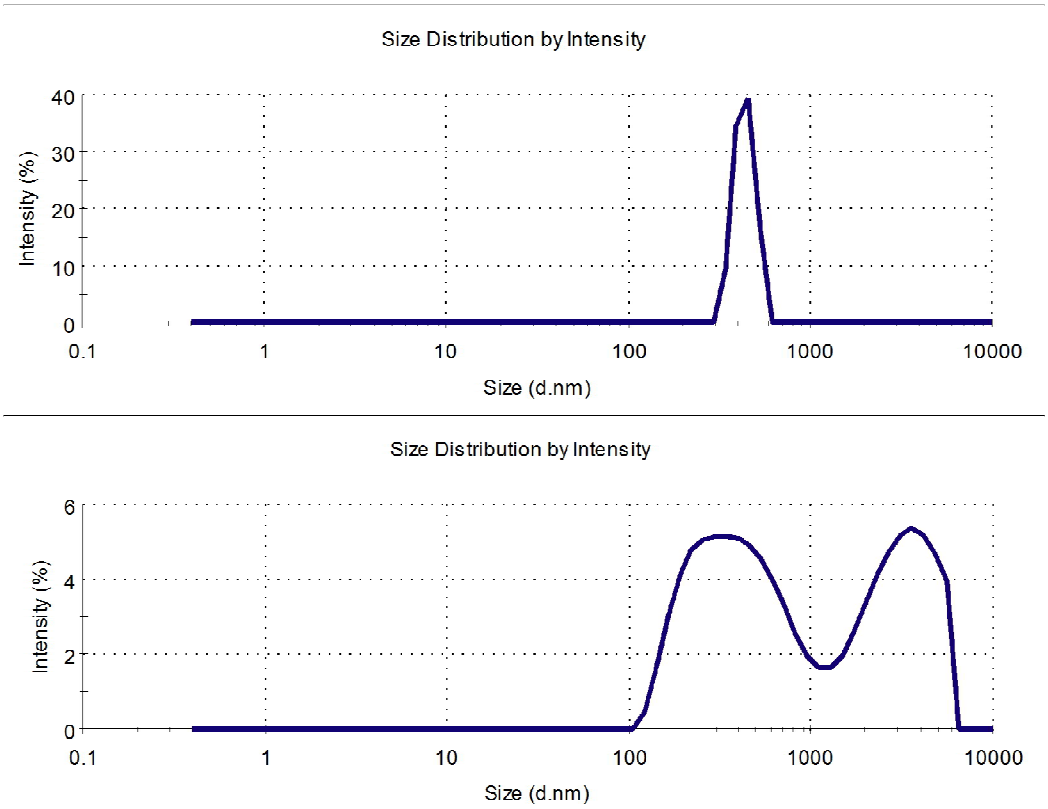

Figure S6. Particle size distribution of DLM@PLGA before and after RF heating *via* DLS method.

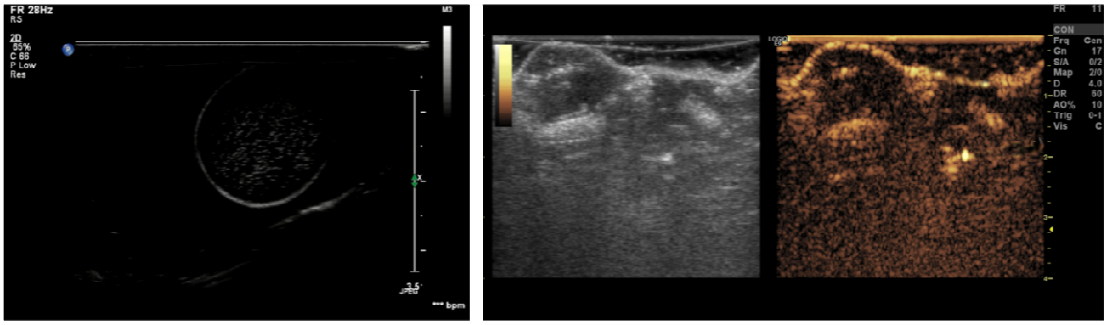

Figure S7. (a) *In vitro* ultrasonic image of free liquid DLM and (b) *in vivo* ultrasonic image of Hela solid tumor after intratumorally injecting free liquid DLM.

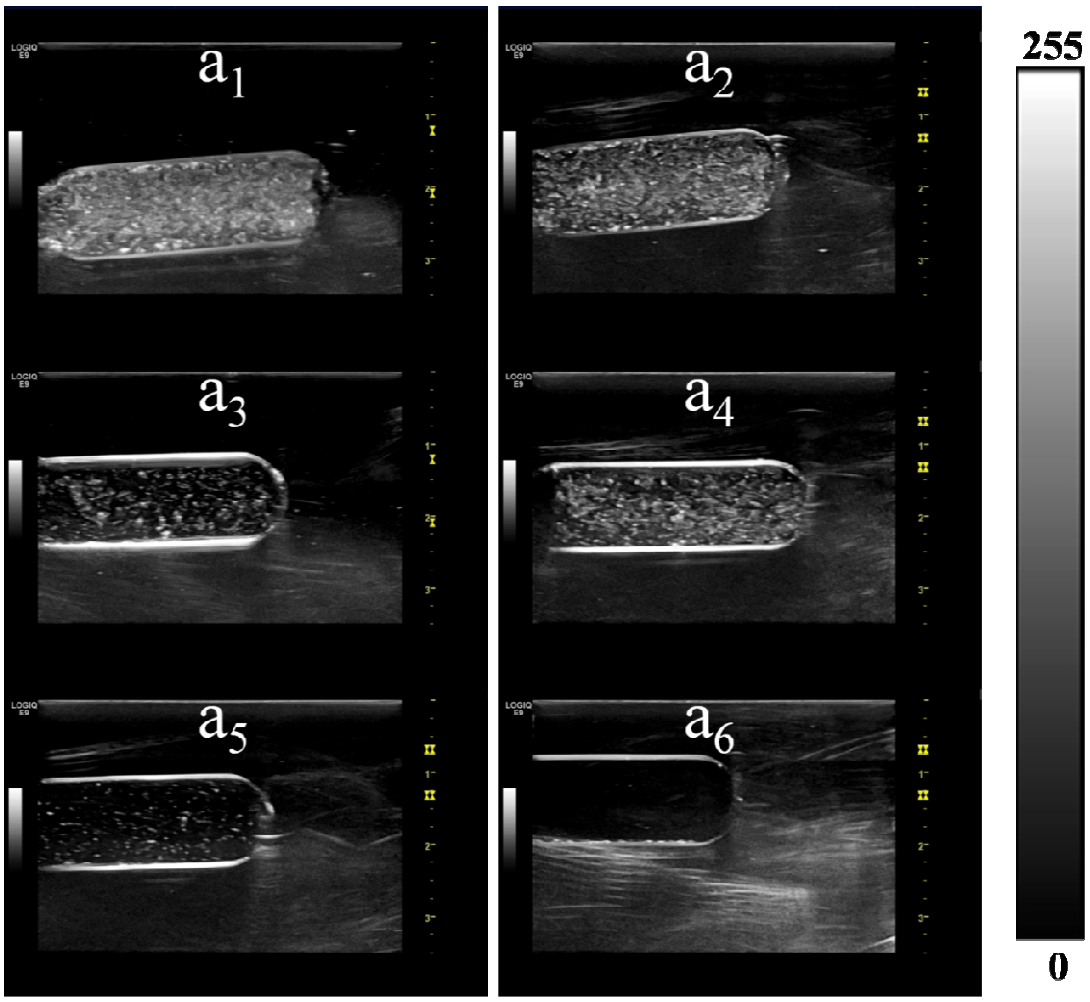

Figure S8. Ultrasonic images of DLM@PLGA after RSV process mediated by RF irradiations with varied mass concentrations of 10 mg/mL (a_1), 8 mg/mL (a_2), 6 mg/mL (a_4), 4 mg/mL (a_3), 2 mg/mL (a_5) and 0 mg/mL (a_6).

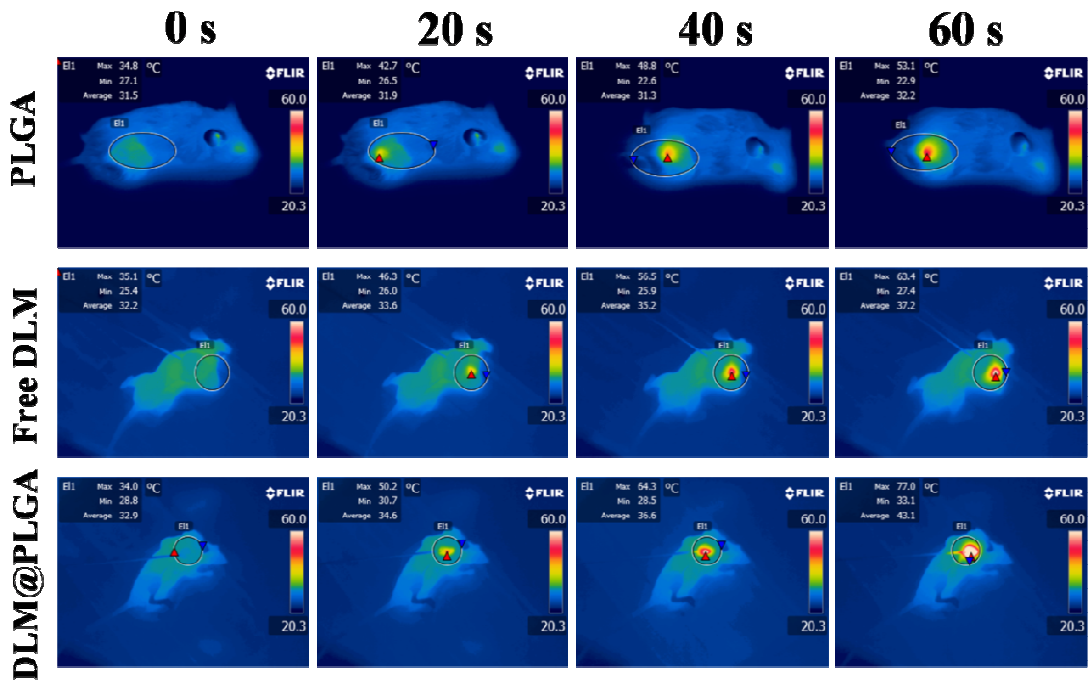

Figure S9. *In vivo* thermal infrared images of Hela xenografted tumor implanted female nude mice after intratumorally injecting PLGA dispersion, free liquid DLM and DLM@PLGA dispersion, which can monitor the *in vivo* temperature variation as a function of irradiation time.

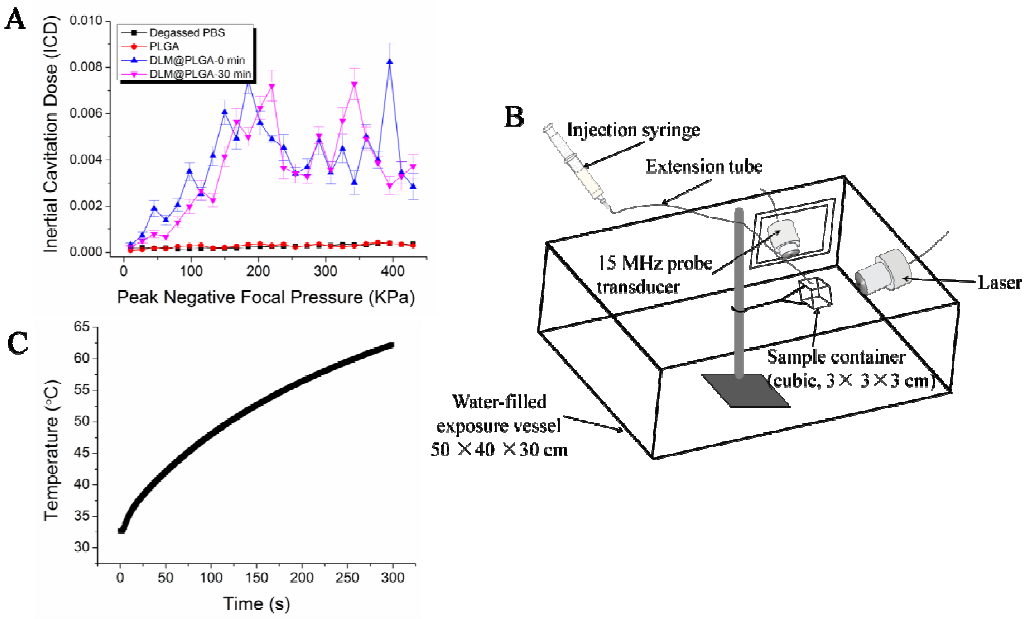

Figure S10. Measurement of inertial cavitation dose (ICD) characterizing inertial cavitation. (A) Inertial cavitation dose (ICD) of PBS, PLGA and DLM@PLGA instantly measured once exposure to laser irradiations and 30-min delay.

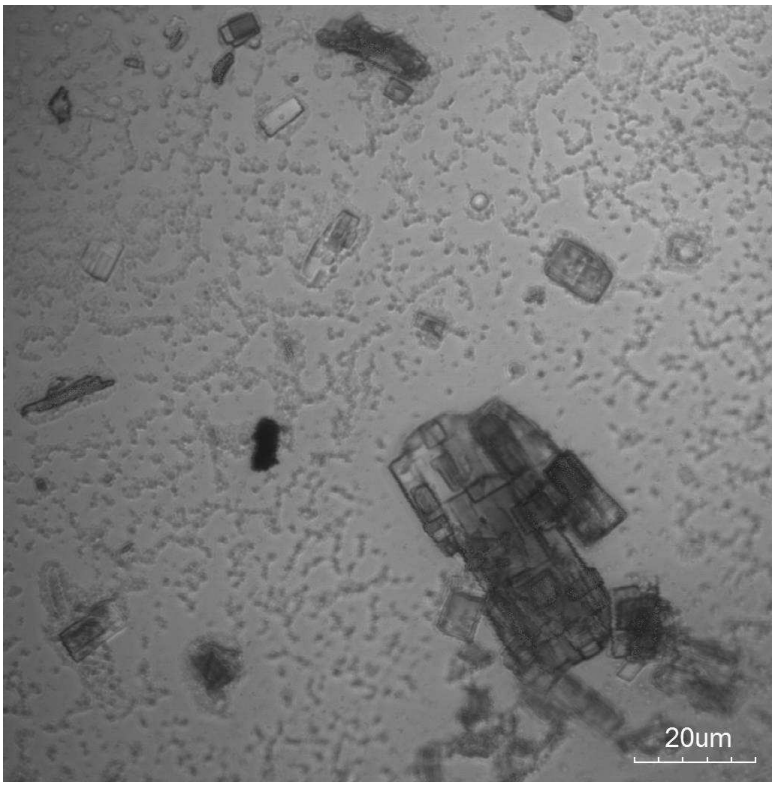

Figure S11. Bright-field confocal image of the mixture consisting of free Liquid DLM and DLM@PLGA nanocapsules dispersed in PBS, and the mixture was subjected to drastic ultra-high velocity homogenization.

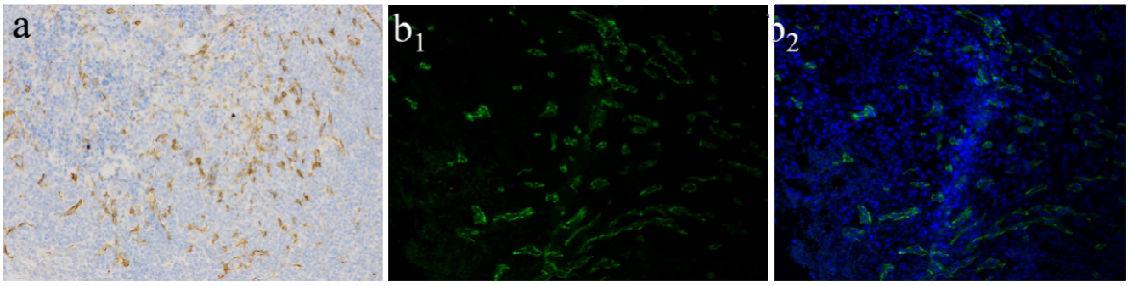

Figure S12. (a) Optical microscopic image of Hela solid tumor stained by CD34 immunohistochemistry, and the matured vessels was stained by brown color (positive expression); (b_1,b_2) Confocal microscopic images of Hela solid tumor stained by FITC-CD31 immunofluorescence, notes: b_1 is the FITC channel that direct represents CD31 expression and reflect the newborn vessels, and b_2 is the merged channel of FITC and DAPI that stained cell nuclei.

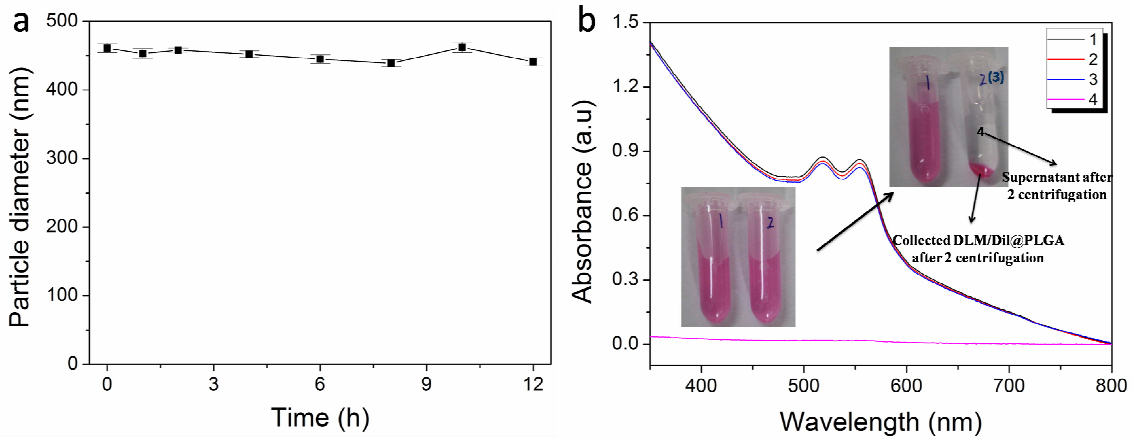

Figure S13. (a) Time-dependent size distribution of DLM/Dil@PLGA nanocapsules obtained *via* DLS method, and no evident size variation suggests the excellent structural stability of DLM/Dil@PLGA nanocapsules. (b) Uv-vis spectra and digital photos of DLM/Dil@PLGA nanocapsules with different treatments: 1 represents the DLM/Dil@PLGA SBF dispersion at time node= 0 h, 2 represents the DLM/Dil@PLGA SBF dispersion at time node= 12 h, 3 represents the re-dispersion of DLM/Dil@PLGA nanocapsules collected after 2 centrifugation in SBF solution, and 4 represents the supernatant after 2 centrifugation. Negligible UV-vis spectrum difference of 1-3 suggests the no Dil release from DLM/Dil@PLGA nanocapsules, and no evident red color and no characteristic peak of Dil in digital photo and spectrum 4 further demonstrate no Dil disassembly from DLM/Dil@PLGA nanocapsules.

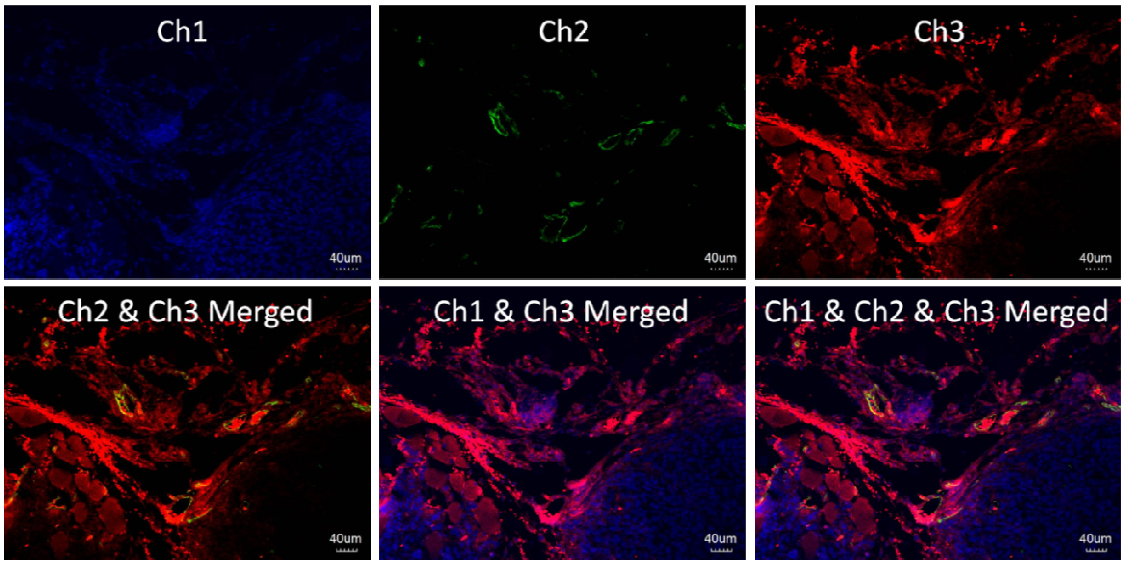

Figure S14. Confocal microscopic images of Hela tumor after intravenous injection of DLM/Dil@PLGA nanocapsules for 2 h, Ch1-Ch3 represent DAPI that characterize tumor cell, CD31-FITC that reflect the vessels in tumor and Dil that reflect the distribution of DLM/Dil@PLGA nanocapsules, and it is clearly found that Dil can traverse the blood vessel and enter intercellular space and even tumor cells from the bottom three merged images.

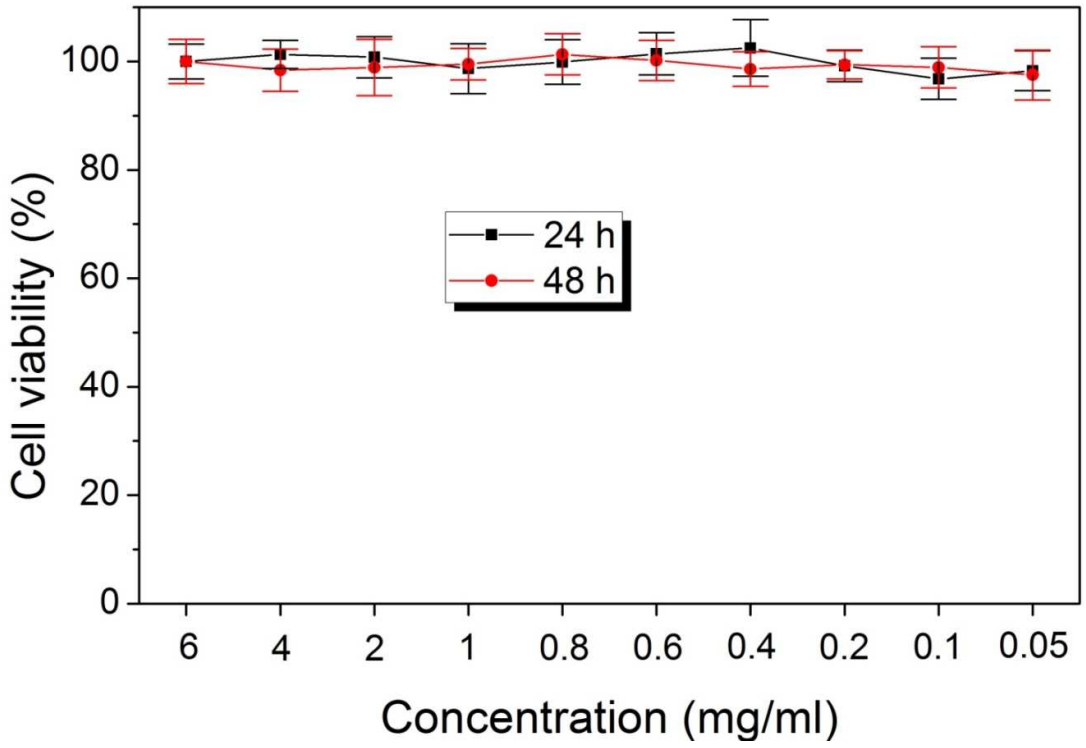

Figure S15. Cell viability of Fibroblast cells L929 treated with different DLM@PLGA nanocapsules for 24 h.

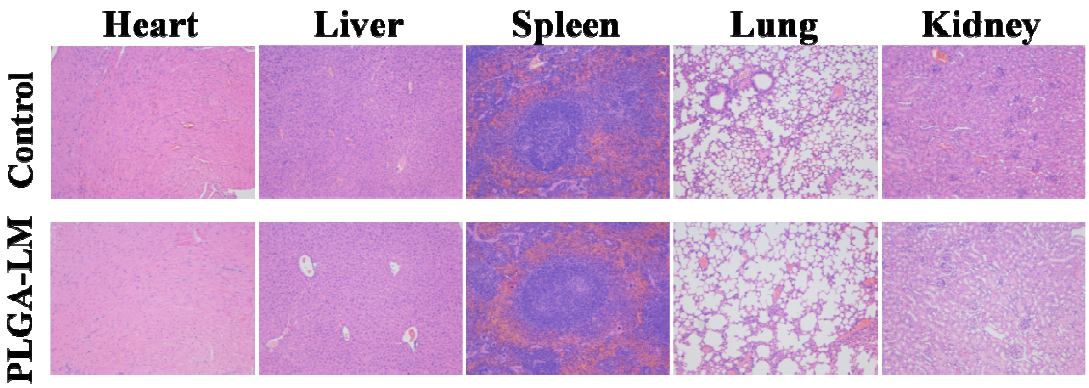

Figure S16. Optical microscopic images of normal organs (heart, liver, spleen, lung and kidney, stained by H&E) of nude mice after intravenously injecting PBS and DLM@PLGA nanocapsules.

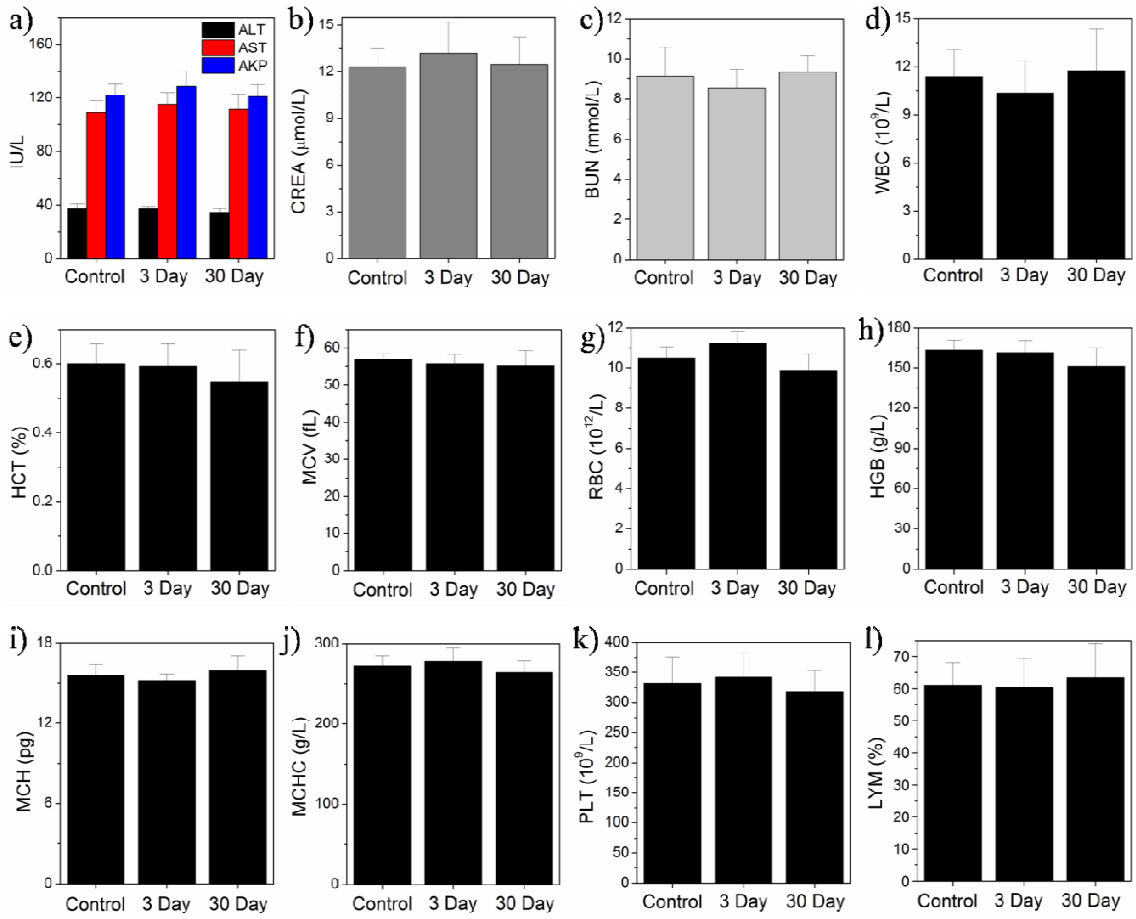

Figure S17. *In vivo* blood and biochemical indexes of nude mice after intravenous injection of DLM@PLGA nanocapsules for different periods.

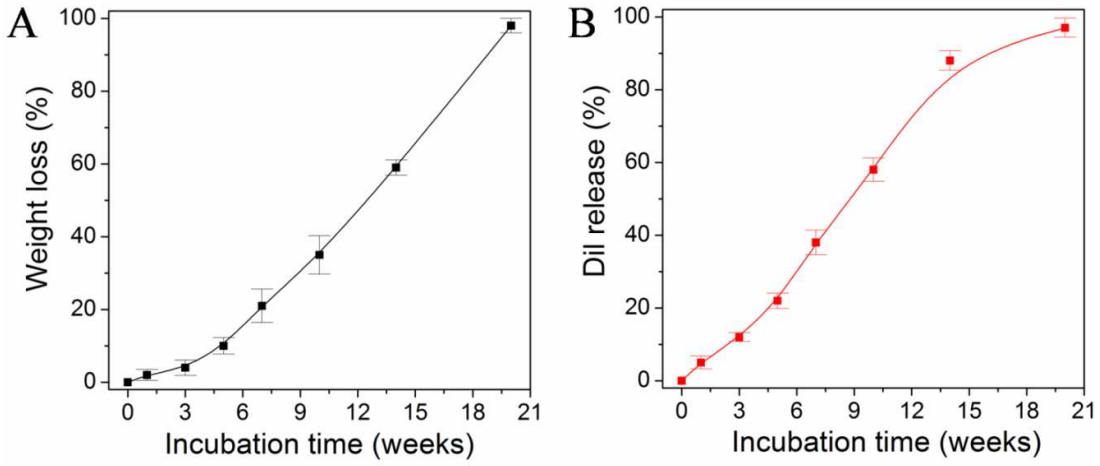

Figure S18. (A) Degradability of DLM@PLGA in simulated body fluid (SBF) solution as a function of incubation time, and (B) Dil release profile from DLM/Dil@PLGA nanocapsules in SBF solution as a function of incubation time.